
UCRL-JRNL-201902

# Performance of the Keck Observatory adaptive optics system

*Marcos A. van Dam, David Le Mignant and Bruce A. Macintosh*

**January 20, 2004**

Applied Optics

This document was prepared as an account of work sponsored by an agency of the United States Government. Neither the United States Government nor the University of California nor any of their employees, makes any warranty, express or implied, or assumes any legal liability or responsibility for the accuracy, completeness, or usefulness of any information, apparatus, product, or process disclosed, or represents that its use would not infringe privately owned rights. Reference herein to any specific commercial product, process, or service by trade name, trademark, manufacturer, or otherwise, does not necessarily constitute or imply its endorsement, recommendation, or favoring by the United States Government or the University of California. The views and opinions of authors expressed herein do not necessarily state or reflect those of the United States Government or the University of California, and shall not be used for advertising or product endorsement purposes.

# Performance of the Keck Observatory adaptive optics system

Marcos A. van Dam,[1] David Le Mignant[2] and Bruce A. Macintosh[1]

[1] Lawrence Livermore National Laboratory, P. O. Box 808, Livermore, CA 94550
[2] W. M. Keck Observatory, 65-1120 Mamalahoa Highway, Kamuela, HI 96743

In this paper, the adaptive optics (AO) system at the W. M. Keck Observatory is characterized. We calculate the error budget of the Keck AO system operating in natural guide star mode with a near infrared imaging camera. By modeling the control loops and recording residual centroids, the measurement noise and bandwidth errors are obtained. The error budget is consistent with the images obtained. Results of sky performance tests are presented: the AO system is shown to deliver images with average Strehl ratios of up to 0.37 at 1.58 $\mu$m using a bright guide star and 0.19 for a magnitude 12 star.

**OCIS codes:** 010.1080,010.1330,010.7350

## 1. Introduction

Adaptive optics (AO) has found widespread use in astronomical settings to compensate for atmospheric turbulence and telescope aberrations.[1–3] At the W. M. Keck Observatory, there are identical adaptive optics systems on the Keck I and Keck II telescopes.[4] Keck I is used only for interferometry and hence does not have a science camera, while Keck II supports a number of instruments. This paper characterizes the performance of the Keck II adaptive optics system operating with a natural guide star when used with the NIRC2 (near infrared) camera in imaging mode. The performance of the Keck I adaptive optics system is very similar.

Characterization of AO systems has been undertaken at other observatories.[5–8] It is important to understand the performance of the AO system under different atmospheric conditions and guide star brightnesses in order to predict the science output of an observation. It is also a good exercise to perform in conjunction with an AO optimization effort: knowledge of the error terms leads naturally to their elimination or mitigation. Finally, understanding the performance of current AO systems will lead to better design and implementation of future systems.

The remainder of the paper is as follows. Section **2.** outlines the Keck AO system and its components. This is followed by an error budget in Sect. **3.**, experimental results in Sect. **4.** and conclusions are drawn in Sect. **5.**.

## 2. Keck adaptive optics system

In this section, the components of the Keck AO system are described and analyzed. In particular, factors that affect performance are emphasized.

The Keck AO system consists of a tip/tilt mirror (TT), a 349-actuator Xinetics deformable mirror (DM) and a dichroic beamsplitter that directs the visible light to the 20×20 subaperture Shack-Hartmann wave-front sensor (WFS) and the infrared light to the science camera. There are also two control loops driving the TT and DM.

The fact that the Keck telescope is on an alt/az mount with the adaptive optics system on a Nasmyth platform means that as the telescope tracks a star, the image rotates on the science camera. To compensate for this, there is an image rotator located before the AO system, which keeps the image steady as the telescope tracks an object but causes the pupil to rotate on the wave-front sensor camera and on the DM. Because the pupil is not circular, but a serrated hexagon, the illuminated subapertures change with time. At any given time, 240 out of the 304 subapertures are active and used to reconstruct the wave-front. The other subapertures are discarded as they have little or no illumination.

The science camera is a 1024×1024 pixel infrared camera with numerous filters. It also has spectroscopic and coronographic capabilities. The camera has a sub-arraying capability that can be used to reduce the exposure time to as short as 8 ms with three seconds between consecutive exposures. The plate scale can be selected to be 10, 20 or 40 milliarcseconds.

In addition to science camera images, there are two other forms of data at our disposal to characterize the AO system. Telemetry consists of the values of any quantity used by the AO system and is streamed at a rate of 10-20 Hz. This is useful for detecting trends over long periods of time. Telemetry is used by the AO system for many operations, such as off-loading focus to the telescope. Diagnostics refers to 1000 consecutive samples of the output of most values calculated by the wave-front controller, such as the centroids and the voltage applied to the DM or TT. Writing the diagnostics to disk typically takes about 10 seconds, depending on how much data is stored.

There is also an atmospheric characterization tool that estimates Fried's parameter, $r_0$,[9] from open- or closed-loop telemetry or diagnostics online.[10]

## A. CCD

The wave-front sensing CCD is a Lincoln Labs MIT 64×64 CCD. The readout electronics consists of four amplifiers, one for each of four 64×16 strips. There are 3×3 pixels corresponding to each subaperture, consisting of a 2×2 pixel quad cell with a guard band between adjacent subapertures. In order to compute the error in estimating the centroid of the WFS spots, some physical parameters of the CCD need to be determined.

### *1. ADU per electron*

The CCD intensities are not measured in photons but in analogue-to-digital units (ADUs). The probability distribution of the number of photons detected by the CCD obeys Poisson statistics, with the variance being equal to the expected number of photons. This property is used to compute the electrons per ADU conversion factor. Wave-front sensing images were captured at the highest frame rate with different neutral density filters. Each frame was normalized to remove overall intensity fluctuations between frames with the same filter. It can be assumed that the variation from frame to frame is due to intensity fluctuations in the light source rather than the fluctuations in photon detection. Then the images were flat-fielded. The slope of the graph of the variance of the pixel intensities versus the mean pixel intensity gives the inverse of the electrons per ADU factor, which takes a value of 1.99.

### *2. Linearity*

The CCD has two amplifier gains. The most commonly used mode has a gain of 1.99 electrons per ADU. The other mode, which has a gain of 4.00 electrons per ADU, is only used on the brightest

stars. Saturation of the WFS CCD occurs about 2000 ADU per pixel, corresponding to a guide star of magnitude 4.5. For brighter stars, a neutral density filter may be used to limit the light on the wave-front sensor.

The third of the four CCD amplifiers exhibits non-linear behavior. The ADU/electron ratio for that CCD strip increases gradually from about 60% of its maximum value in the limit where there is no light, to almost 100% at about 150 counts per ADU. Since the read noise in electrons does not change, the effect of the read noise is greater. We have ensured that no subaperture is straddled by the third CCD strip and a neighboring one.

*3. Dark current*

To find the dark current, dark frames were captured at different frame rates. The mean intensity was recorded and plotted as a function of exposure time. The slope of the graph gives the dark current, 4470 electrons/pixel/second. Dark current is strongly dependent on temperature and the CCDs are Peltier cooled to 267 K (-6° C). The measured dark current is consistent with its theoretical value:

$$I_{\rm dark} = AT^{3/2} \exp[-E_g/2kT], \tag{1}$$

where $I_{\rm dark}$ is the dark current, $E_g = 1.2$ eV is the silicon band gap energy, $T$ is the temperature in Kelvin, $k$ is Boltzmann's constant and $A$ is a proportionality constant equal to $2.15\times10^8$ $e^- s^{-1}\text{pixel}^{-1}K^{-3/2}$ according to Lincoln Labs.

*4. Read noise*

For a dark frame at 672 Hz, the dominant signal is read noise. Removing the contribution from the dark current, we obtain a read noise standard deviation of 6.5 electrons/pixel/readout.

### B. Lenslets

The lenslets are 20×20 acrylic lenslets from Adaptive Optics Associates with a pitch of 200 $\mu$m. There are three sets of lenslet arrays available, with focal lengths of 2.0, 5.0 and 7.9 mm, corresponding to design plate scales of 2.44, 0.98 and 0.62 arcsec/pixel respectively. The measured plate scales, however, are 2.4, 0.8 and 0.5 arcsec/pixel.

The WFS spot size is a very useful quantity to determine because it is needed to convert the centroid measurements into angles-of-arrival. Knowing how the size of the spot changes due to turbulence is very important to eliminate dynamic calibration errors, optimize the loop gains and calculate the measurement noise and bandwidth errors.

To find the size of the spots on the WFS, we displace the spot over a range of values and measure the centroid, as shown on Fig 1. The maximum slope, $m$, of the "displacement in arcseconds versus centroid" plot is related to the full-width-half-maximum (FWHM) of a Gaussian spot by

$$\text{FWHM} = \frac{2 \times 2.355}{\sqrt{2\pi}m}. \tag{2}$$

The spot can be shifted by scanning the artificial light source across the focal plane and measuring the centroids.[10] The displacement of the spot is found by multiplying the displacement of the light source by the plate scale at the focal plane. An alternative way of scanning the spot is to close the DM and TT loops and add a range of constants between, say, -0.1 to 0.1 to all of the x (or y) centroid offsets. The displacement of the spot is then measured with the science camera, which has an extremely well calibrated plate scale. The latter method has the advantage that it can also be used to measure the spot size on the sky using a guide star.

The FWHM spot sizes on the light source were found to be 1.25, 0.52 and 0.40 arcsec for the 2.4, 0.8 and 0.5 arcsec plate scales respectively. This compares with a diffraction-limited spot size

Fig. 1. Transfer curve between the angle-of-arrival in arcseconds and the mean centroids. The plot is generated by displacing the white light source in the y-direction.

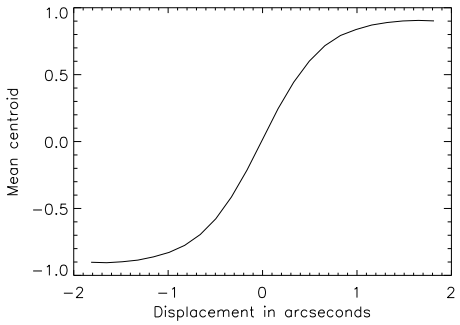


of 0.23 at 700 nm. The discrepancy is well explained by postulating that the measured intensity is a convolution of a diffraction-limited spot and a Gaussian with a FWHM of half a pixel. The blurring of the spot is almost certainly due to charge diffusion and the extent of the charge diffusion is consistent with other measurements of similar CCDs.[12] The effect of the charge diffusion on the spot size increases with increasing plate scale.

Under average seeing conditions ($r_0$=20 cm), the average spot size increases relative to the spot using the white light source by 25% and 70% for the 2.4 and 0.8 arcsec plate scales.

Usually, the 2.4 arcsec plate scale lenslets are used, because the spot size does not change angular extent much in the presence of turbulence. Also, essentially all the light is detected by the quad cells and does not leak out. However, the larger the angular extent of the spot, the higher the noise on the wave-front slope estimates. Although the error in the centroid estimate is independent of spot size, the wave-front slope corresponding to this error is inversely proportional to the spot size. Hence, when the guide star is faint and the seeing is relatively good, the 0.8 arcsec plate scale is preferred. The 0.5 arcsec plate scale is never used.

When the DM is nominally flat, the RMS centroid measurements are 0.11 centroids (0.068 arcsec) on the 2.4 arcsec plate scale and 0.13 centroids (0.028 arcsec) on the 0.8 arcsec plate scale. These centroid errors are randomly distributed and are believed to stem from the lenslets themselves. As a result of these aberrations and also aberrations on the science camera leg, the wave-front sensor operates off null. The penalties paid for operating off null are an increase in noise because the WFS is no longer operating in the steepest part of the transfer curve (Fig. 1) and dynamic calibration errors explained in Sect. **3.F.** due to the changing spot size.

The corners of the lenslets are optically conjugate to the four neighboring actuators in what is commonly called the Fried configuration.[11]

### C. Deformable mirror

The Keck AO system consists of a Xinetics 349-actuator deformable mirror (DM). Oppenheimer *et al.* investigated the influence function of this mirror.[13] The influence function describes the optical effect of the deformation of the mirror when one volt is applied to the pre-amplifier. It has been calibrated at Keck Observatory in three ways: by measuring the wave-front directly with an interferometer, by reconstructing the wave-front from the centroids when an actuator is poked and by adding a known defocus and reading the position of the actuators. The influence function,

$S(x,y)$, can be well approximated using the difference of two Gaussians:

$$S(x,y) = \left( \frac{w_1}{2\pi\sigma_1^2} \exp\left[\frac{-(x^2+y^2)}{2\sigma_1^2}\right] + \frac{w_2}{2\pi\sigma_2^2} \exp\left[\frac{-(x^2+y^2)}{2\sigma_2^2}\right] \right) \times 0.470\ \mu\text{m}. \quad (3)$$

The values for the constants are: $w_1 = 2$, $w_2 = -1$, $\sigma_1 = 0.54$ subapertures and $\sigma_2 = 0.85$ subapertures. It is apparent that the behavior of the DM is more complex than a linear sum of the influence functions of the actuators. For example, if all the actuators have the same voltage applied the DM produces piston, which is not predicted by Eq. (3).[25]

### D. Calibration

Calibrating an AO system well is crucial to obtain good performance on the sky. Here, a brief description of the most important calibration procedures is presented with some procedures reported in more detail elsewhere.[15] The calibrations are performed using a white light source that is 10 $\mu$m (13.8 milliarcsec) in diameter and located at the focus of the telescope.

#### *1. DM to lenslet registration*

It is important to have the correct registration between the DM and the lenslet. Otherwise, the waffle mode, where actuators are lined up in a checkerboard pattern, would be observed on the DM when the the loop is closed. The algorithm used to perform the DM-to-lenslet registration is adapted from a paper by Oliker.[14] It involves putting waffle on the DM and moving the lenslets so as to minimize the the signal sensed by the WFS.

#### *2. Focusing the WFS CCD*

Previously, the CCD was focused by defining the focus to be the position of the CCD where the steepest transfer curve (see Fig. 1) occurs. It is easy to show that this is indeed the best focus when there is no charge diffusion on the CCD but differs greatly from the true focus in the presence of charge diffusion. Instead, a waffle pattern is introduced into the DM. This is equivalent to adding 45° astigmatism to each lenslet. If the CCD is out of focus, then the spots on the WFS will be elongated along one diagonal and not the other. At the best focal position, the spots will be symmetrical.

#### *3. System matrix generation*

The system matrix relates the motion of each actuator to the centroids produced at the WFS. It is calculated by moving each actuator by $\pm 0.2$ $\mu$m and recording the difference in the centroids. Centroids corresponding to subapertures that are more than twice the subaperture spacing away from the actuator are set to zero to reduce the level of noise. The actuator motion is chosen such that it yields a good signal-to-noise ratio in the centroid measurements while ensuring that the the WFS is operating in its linear range.

#### *4. Image sharpening*

There are aberrations on the imaging leg that are not sensed by the WFS and vice versa. In the absence of any external aberrations, one would want the DM to have the shape that maximizes the Strehl ratio. Image sharpening refers to the process of finding this optimum shape of the DM. The non-common path aberrations are calibrated as follows. First, the DM is flattened using a WYKO phase-shifting interferometer: The phase on the DM is measured with the interferometer and a voltage applied is to cancel the measured phase.[15] Unfortunately, the interferometer does not see some of the actuators at the edges and these cannot be flattened properly. Next, the phase diversity algorithm of Loefdahl and Scharmer[16] is employed to remove the Zernike polynomials[17] up to $Z_{15}$.

Typically, 100 nm of RMS wave-front are applied to the DM in order to correct for any aberrations in the imaging leg and in the common path. The algorithm reduces the total wave-front error seen on the artificial source from 150 nm to 113 nm. These numbers take into account the finite size of the source. The phase diversity algorithm is only applied to images taken at one location in the camera using one filter. Hence, there are additional field- and filter-dependent wave-front errors.

Once the optimum shape is found, it is placed on the DM and the centroids measured by the wave-front sensor are defined to be the centroid origins. In closed-loop operation, the DM and TT mirror are driven in such a way to null the difference between the centroids and the centroid origins. Hence, upon immediately closing the loops, the DM should not move.

Under average atmospheric conditions ($r_0 = 20$ cm), the spot obtained using the 2.4 arcsec/pixel plate scale increases in size from 1.25 arcsec to 1.55 arcsec. Before going to the sky, the centroid offsets are scaled by 0.8 to account for the increase in spot size. If the beacon is an extended source, such as a planet, or if the 0.8 arcsec/pixel plate scale is used, then the centroid offsets are scaled even more. Unfortunately, the spot size is constantly changing as the seeing changes. It is intended that in the near future, the spot size will be monitored in real time using telemetry readings of the DM voltages.[18]

### E. Signal processing

#### *1. Reconstruction matrix*

As previously mentioned, the pupil rotates as the telescope tracks an object and the illuminated subapertures change with time. Every time the pupil rotates one degree, the calculation of a new reconstruction matrix is triggered. Until recently, the matrix inversion of the influence matrix, $H$, was performed using an SVD algorithm.[19] This has been replaced by a Bayesian reconstructor that uses the covariances of Kolmogorov turbulence, $C_\phi$ and the relative noise in subaperture, $W$, as prior information. There is a parameter, $\alpha$, that can be adjusted depending on the signal-to-noise ratio. The reconstructor, $R$, is given by[20]

$$R = (H^T W^{-1} H + \alpha C_\phi^{-1})^{-1} H^T W^{-1}. \tag{4}$$

This would be the optimal reconstructor in the open-loop case; simulations and extensive sky testing have demonstrated that it also performs very well in closed loop. The reason why it works well is that the inversion of the system matrix is regularized, so that noise in the centroids leads to smaller actuator motions. The new reconstructor has resulted in an increase in the Strehl ratio corresponding to the elimination of 100 nm of wave-front error (in quadrature) for bright guide stars. The most salient difference is the elimination of the four spots in a square pattern in the image indicative of unsensed waffle on the DM. The magnitude of the improvement increases as the guide stars get fainter, because $\alpha$ is increased to further suppress the noise at the expense of suppressing some signal.

#### *2. Frame rate and delay*

The wave-front controller can operate at frame rates in the range of 55 to 672 Hz. The upper limit is set by the combination of the camera readout time and the speed at which the computers can multiply the reconstructor matrix by the centroid measurements. There are separate control loops for the TT and the DM. The compute delay times, from the time that the CCD is read until the time that the TT and DM voltages are updated, are 1.65 ms and 2.13 ms respectively.

*3. Loop gains and compensator*

Each of the control loops has its own controller. The TT loop is a straight integrator with a variable loop gain, $k_{\mathrm{TT}}$, and a fixed gain scaling of 0.8:

$$y[n] = y[n-1] + 0.8k_{\mathrm{TT}}u[n], \tag{5}$$

where $y[n]$ is the output from and $u[n]$ is the input to the controller at time $n$. The transfer function can be written as

$$H_{\mathrm{TT}}(z) = \frac{0.8k_{\mathrm{TT}}z}{z-1}, \tag{6}$$

where $z$ is the complex Z-transform variable. The DM loop has a double pole compensator with the following temporal response:

$$\begin{aligned} e[n] &= -we[n-1] + k_{\mathrm{DM}}u[n] & (7)\\ y[n] &= ly[n-1] + e[n], & (8) \end{aligned}$$

where $e[n]$ is an intermediate quantity. The transfer function is

$$H_{\mathrm{DM}}(z) = \frac{k_{\mathrm{DM}}z^2}{(z-l)(z+w)}. \tag{9}$$

The compensator, whose function is to increase the bandwidth of the controller,[21] has its weight, $w$, set to 0.25. The leak factor, $l$, set to 0.999 for bright stars and 0.99 otherwise, ensures that invisible modes do not build up in the DM. The loop gain, $k_{\mathrm{DM}}$, is also variable.

The optimum loop gains depend on the turbulence strength and speed, the extent and brightness of the guide star and the frame rate. In routine operation, the loops gains and the frame rate are set using a look-up table that has the median number of ADUs per subaperture per second as its only input. We plan to implement real-time gain optimization using centroid telemetry.

## 3. Error budget

### A. Strehl ratio

A figure of merit often used to characterize the error of an AO system is the Strehl ratio, $S$. It is defined as the ratio of the maximum value of the measured point-spread function over the maximum value of the diffraction-limited point spread function. The Strehl ratios of all the images were calculated using a window with a diameter of 2 arcsec.

The Strehl ratio is related to the wave-front errors via the Maréchal approximation,[3]

$$S = \exp[-\sigma_\phi^2]\exp[-\sigma_\chi^2], \tag{10}$$

where $\sigma_\phi^2$ is the wave-front phase variance and $\sigma_\chi^2$ is the variance of the log-normal amplitude at the pupil plane. An AO system with a single wave-front corrector conjugate to the ground can only correct the wave-front phase aberrations. Hence the goal of the AO system is to minimize the wave-front error. In this section, the individual wave-front error terms are presented. The phase error is inversely proportional to the wavelength, so the Strehl ratio increases with increasing wavelength. In engineering tests, the filter used was H continuum, a narrow band filter centered at 1.58 $\mu$m with a 1% passband. A short wavelength enables one to more easily discern performance changes in real time, as the image quality varies more than for the longer wavelengths. All Strehl ratios quoted in this paper correspond to 1.58 $\mu$m. Strehl ratios at other wavelengths can be estimated using Eq. (10). All the wave-front errors are root-mean-squared (RMS) errors.

### B. Scintillation

The result of propagating an aberrated wave-front from height $h$ above the telescope to the primary mirror of the telescope is that the wave-front aberrations, when propagated, give rise to changes in the amplitude of the wave. Consider the atmospheric turbulence to be located at a single layer so that the $C_n^2$ profile can be written as a delta function at height $h$. Then, for an infinite aperture, it can be shown that the log-normal amplitude variance is given by[22]

$$\sigma_\chi^2 = 0.563 k^{7/6} h^{5/6} C_n^2(h), \tag{11}$$

where $k = 2\pi/\lambda$ is the wavenumber. Using the relationship

$$r_0 = \left(0.423 k^2 C_N^2(h)\right)^{-3/5} \tag{12}$$

we obtain

$$\sigma_\chi^2 = 0.288 \left(\sqrt{\lambda h}/r_0\right)^{5/3}. \tag{13}$$

Analytic calculations[22] and numerical simulations by the authors using Fresnel propagation both show that this result also holds for large astronomical telescopes.

As an example, consider the hypothetical case of a turbulent layer with an $r_0$ value of 20 cm at 500 nm and 80 cm at 1.58 $\mu$m located 3 km above the ground. Substituting into Eq. (13) gives $\sigma_\chi^2 = 0.0048$. The reduction in Strehl, using Eq. (10), is 0.48%. Since virtually all the atmospheric turbulence is below a height of 10 km and the log-amplitude variance depends on $h^{5/6}$, we conclude that the effect of scintillation is negligible compared to that of the wave-front phase.

### C. Camera errors

The Strehl ratio measured on the artificial light source after image sharpening is 0.77, corresponding to 130 nm of wave-front error. However, the light source can be resolved and its extent reduces the Strehl by the same amount as 64 nm of wave-front aberrations. Hence, the actual wave-front error is 113 nm. Figure 2 shows the phase error after image sharpening computed using the Gerchberg-Saxton phase retrieval algorithm.[23] Because of the symmetry of the aperture, there is an ambiguity about the sign and the orientation of the phase so it is difficult to feed back this information in the image sharpening process.[24] It can be seen that most of the residual error consists of high-order aberrations. We intend to use this information to improve the image quality.

Fig. 2. Phase map of the residual error after image sharpening.

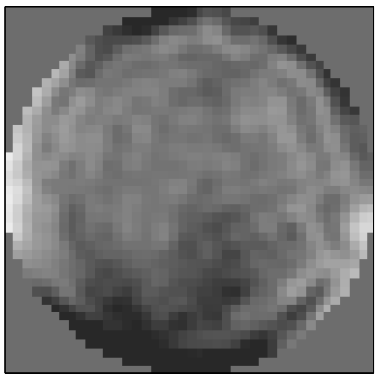

### D. Fitting error

The fitting error is defined to be the component of the wave-front that cannot be corrected by the deformable mirror. There are two sources of error that the DM has to correct for: the atmospheric turbulence and the telescope error. This error depends on the spacing between the actuators, the influence function of the actuators, the spatial power spectrum of the wave-front aberrations induced by the turbulence and the telescope.

Using the influence function described by Eq. (3), it was found by simulation that the RMS fitting error, $\sigma_{\mathrm{FIT}}$, for Kolmogorov turbulence is equal to $33.2 r_0^{-5/6}$ nm. The general form of the fitting error is given by[3]

$$\sigma_{\mathrm{FIT}} = \sqrt{a_f} \left( \frac{d}{r_0} \right)^{5/6} \frac{\lambda}{2\pi}, \tag{14}$$

where $d$ is the spacing between the actuators, $\lambda$ is the wavelength at which $r_0$ is measured and $a_f$ is a constant that depends on the influence function. The value of $a_f$ calculated here is 0.46, which is higher than the range of 0.28 to 0.34 presented in Hardy for a continuous-plate mirror.[3]

The Keck primary mirror consists of 36 hexagonal segments. Each segment has low-order aberrations and a dimple in the center resulting from the manufacturing process. In addition, there are stacking (piston) and pointing (tip/tilt) errors of each segment relative to its neighbors. It is estimated that after phasing the mirror segments,[26] there are about 110 nm of wave-front residual error. The telescope fitting error, $\sigma_{\mathrm{TEL}}$, after correction by the DM was found to be 60 nm by simulating the errors on the primary mirror of the telescope: It is not possible to correct well for the segment discontinuities. The segments are not routinely phased before an AO run so this error could be higher.

### E. Bandwidth and noise errors

The bandwidth errors are due to the finite sampling rate of the atmospheric turbulence and the delay between the centroid measurements and the DM and TT command updates. The source of the noise errors is the uncertainty in the centroid estimates due to the finite number of photons on the WFS. To calculate these error terms, a good model of the temporal response of the control loop is required.

#### *1. Modeling the dynamic performance of the AO system*

The wave-front controller is described in detail in Johansson *et al.*[27] and the features of the controller required in the model are simply stated here. A schematic of the TT and DM feedback loops for the Keck AO system is displayed in Figure 3. Both loops have a similar form, but the compensators and the compute delays differ.

The transfer functions of the individual blocks are as follows:[21]

- Camera stare and the zero-order hold with period $T$:

$$H_{\mathrm{STARE}}(s) = H_{\mathrm{ZOH}}(s) = \frac{1 - \exp[-sT]}{sT}. \tag{15}$$

- Compute delay with delay time $\tau_c$:

$$H_{\mathrm{DELAY}}(s) = \exp[-s\tau_c]. \tag{16}$$

The compensator block is modeled by substituting $z = \exp[sT]$ into the discrete compensator of Eqs. (6) and (9). In the above equations, $s = i2\pi f$ is the complex frequency variable and $f$ is the

Fig. 3. Schematic of the control loop. The diagnostics measure the centroids straight after the addition of the noise and the mirror is driven by the signal coming from the ZOH.

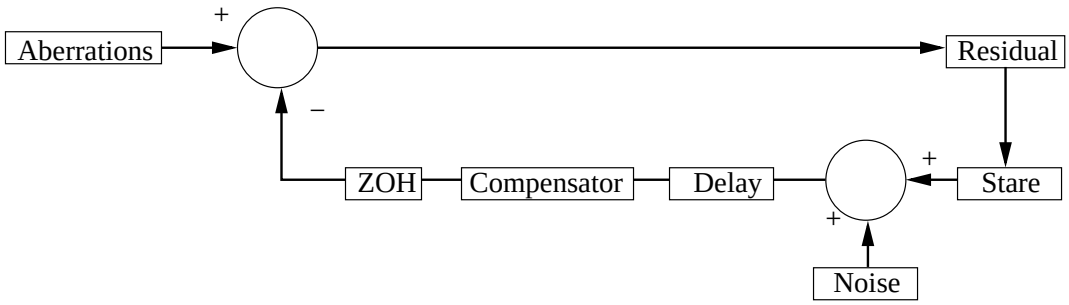


frequency. In what follows, all the blocks will be written with $f$ as the argument, since $f$ has a more intuitive meaning than $s$ and is computed directly from the discrete Fourier transform (DFT) of the diagnostics.

The transfer function of the entire feedback arm of either the TT or DM loop, $H(f)$, can be written as the product of the transfer function of all the blocks:

$$H(f) \quad = \quad H_{\mathrm{STARE}}(f)H_{\mathrm{DELAY}}(f)H_{\mathrm{TT/DM}}(f)H_{\mathrm{ZOH}}(f). \tag{17}$$

There are two inputs into the control system: the noise, $N(f)$, which is assumed to have the same power at all temporal frequencies and the turbulence, $X(f)$. Likewise, there are two outputs, the mirror position, $M(f)$, and the residual mirror commands obtained from the diagnostics, $D(f)$. The position of the diagnostics in the control loop is just after the addition of the noise, while the mirror position is just after the zero-order hold. The residual DM commands are obtained by matrix multiplying the reconstruction matrix with the residual centroids. Likewise, the residual TT commands are obtained by taking the average of the x and y centroids. For notational simplicity, we consider the noise to be input before, rather than after, the stare. This assumption has little impact on the transfer functions of the control loops.

The transfer function relating the the mirror position to the the turbulence and noise is

$$M(f) = \frac{H(f)}{1+H(f)}(X(f)+N(f)), \tag{18}$$

while the diagnostics power spectrum is given by

$$D(f) = \frac{1}{1+H(f)}(X(f)+N(f)). \tag{19}$$

The measurement noise wave-front error, $\sigma_{\mathrm{NOISE}}$, is due to noise in the centroid measurement propagating to the mirror, $N(f)H(f)/(1+H(f))$. The square of its value is

$$\sigma^2_{\mathrm{NOISE}} = \int_{-\infty}^{\infty} \left|\frac{H(f)}{1+H(f)}\right|^2 |N(f)|^2 \mathrm{d}f. \tag{20}$$

Since the noise only has power at discrete frequencies, Eq. (20) can be rewritten as

$$\sigma^2_{\mathrm{NOISE}} = \sum \left|\frac{H(f)}{1+H(f)}\right|^2 |N(f)|^2, \tag{21}$$

where the summation is over all the sampled discrete frequencies.

The bandwidth error, $\sigma_{\rm BW}$, is due to the turbulence that is not compensated by the AO system, $X(f)/(1+H(f))$. The diagnostics measure this term with an added noise term due to the noise on the centroid measurement propagating through the control loop:

$$D(f) = \frac{X(f)+N(f)}{1+H(f)}. \tag{22}$$

Assuming that the noise and the bandwidth errors are statistically uncorrelated, the bandwidth squared error is

$$\begin{aligned}
\sigma^2_{\rm BW} &= \int_{-\infty}^{\infty} \left|\frac{1}{1+H(f)}\right|^2 |X(f)|^2 {\rm d}f \\
&= \int_{-\infty}^{\infty} \left( |D(f)|^2 - \left|\frac{1}{1+H(f)}\right|^2 |N(f)|^2 \right) {\rm d}f \\
&\approx \sum \left( |D(f)|^2 - \left|\frac{1}{1+H(f)}\right|^2 |N(f)|^2 \right).
\end{aligned} \tag{23}$$

It follows that knowledge of the transfer function of the AO loop, $H(f)$, and the power spectra of the diagnostics, $|D(f)|^2$, and of the noise, $|N(f)|^2$, can be used to calculate both the bandwidth and the noise error terms.

*2. Calculating the centroid variance*

In order to estimate the noise and bandwidth errors, we must first derive the error in the centroid estimates. Let $I_1$ denote the background-subtracted intensity of one of the pixels in a quad cell. Then its expected value is

$$\mathrm{E}[I_1] = pT, \tag{24}$$

and, assuming Gaussian statistics, its variance is

$$\mathrm{Var}(I_1) = (p+d+b)T + \sigma_r^2, \tag{25}$$

where $T$ is the integration time, $p$, $d$ and $b$ are the photon, dark current and background fluxes in electrons/pixel/second and $\sigma_r$ is the read noise standard deviation is electrons/pixel/readout. In the analysis that follows, $d = 4470$, $b = 0$ and $\sigma_r^2 = 39.7$. To obtain a simple expression for the variance of the centroid estimates, two simplifying assumptions are made: that there is an equal amount of light in each pixel (*i.e.*, the average centroid is zero) and that the variance of the denominator in the centroid calculation can be neglected. Then the variance of the x (or y) centroid estimate, $c_x$ (or $c_y$), is

$$\begin{aligned}
\mathrm{Var}(c_x) &= \frac{\mathrm{Var(I_1)}}{4\mathrm{E[I_1]}^2} \\
&= \frac{\mathrm{Var(I_1)}}{4(\mathrm{pT})^2} \\
&= \frac{(p+d+b)T + \sigma_r^2}{4(pT)^2}.
\end{aligned} \tag{26}$$

The measured centroid variances agree with Eq. (26). From the variance of the centroids, we can calculate the errors in the TT and DM loops.

*3. Calculating the tip/tilt noise power spectrum*

The tip (or tilt) signal sent to the compensator is the average x (or y) centroid value over the 240 active subapertures. Hence the sum of the variance of the tip and tilt estimates in centroid units is $2\mathrm{Var}(c_x)/240$. The next step is to convert this variance into units of WF error. Using Eq. (2) we obtain the result that 1 arcsec is equivalent to 1.2 centroid units for a spot size of 1.55 arcsec. For the Keck telescope, the RMS WF error due to a tip or a tilt of 1 arcsec is 12.68 $\mu$m. Hence, the TT noise power spectrum is

$$|N_{\mathrm{TT}}(f)|^2 = \frac{2}{240}\left(\frac{12.68}{1.2}\right)^2 \mathrm{Var}(c_x). \tag{27}$$

*4. Calculating the deformable mirror noise power spectrum*

To calculate the deformable mirror noise PSD, we must convert centroid units into wave-front units. The residual centroids are multiplied by the reconstruction matrix, $R$, to convert to voltage commands. The voltage commands are then convolved with the actuator influence function, $S$, to obtain the wave-front induced by the noise. This is achieved using matrix multiplication. Finally, since the size of the WFS spots on the sky increases by 25% relative to their size on the light source, the wave-front must be multiplied by 1.25 (for median seeing conditions with the 2.4" plate scale on the WFS). Since the noise on the actuator voltages are uncorrelated, we can write

$$|N_{\mathrm{DM}}(f)|^2 = 1.25^2 |RS|^2 \mathrm{Var}(c_x). \tag{28}$$

*5. Calculating the bandwidth and noise errors*

To calculate the residual power spectra, the centroids from the diagnostics must be converted into TT and DM wave-front aberrations in exactly the same way as the noise. Then the power spectrum of the diagnostics is taken using the DFT:

$$|D(f)|^2 = |\mathrm{DFT}[d[n]w[n]]|^2, \tag{29}$$

where $w[n]$ is a normalized windowing function used to avoid spectral leakage due to the non-periodicity of $d[n]$, the residual wave-front as measured by the diagnostics. The window must be scaled to have unit power.

The TT and DM noise errors are calculated by inserting Eqs. (27), (28) and (29) into Eqs. (21) and (23).

Plots of the TT and DM power spectral densities averaged over four sets of diagnostics taken on June 15, 2003 are displayed in Fig. 4. The noise on the diagnostics that must be subtracted in to obtain the bandwidth error is superimposed. For this data, the average RMS bandwidth errors were 75 nm for the TT and 103 nm for the DM with corresponding noise terms of 9 nm and 17 nm. The guide star is a 7.2 magnitude star. The power spectral densities are consistent with what was is expected by modeling the transfer function of the system.[27] From the plots of the power spectra, it can be seen that there are vibration peaks at frequencies ranging from 20 to 40 Hz superimposed on Kolmogorov turbulence.

### F. Miscellaneous error

There are several other error terms that have not yet been calculated but should be part of a complete error budget.

The wave-front sensing and reconstruction restrict the performance of the DM. For example, while all the actuators were assumed to be independently controlled in the calculation of the fitting errors, in actual fact many of the actuators have no neighboring subapertures and are slaved to

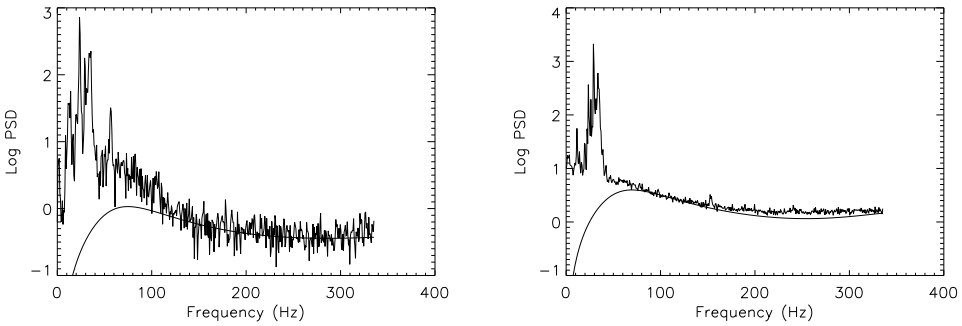


Fig. 4. Logarithm of the power spectral density in $nm^2/Hz$ for the TT (left) and the DM (right). The smooth line represents the noise power on the diagnostics.

the average value of their neighboring actuators. Also, because the wave-front reconstructor has no knowledge of either the influence function of the DM actuators or the analogous response function of the wave-front sensor, even in the absence of noise, the actuators are not driven to their optimum values. Even if the DM had an infinite number of degrees of freedom, there would be an error associated with the finite number of measurements.

Because the wave-front sensor measures the average wave-front slope over the subaperture, any wave-front aberrations with a spatial frequency higher than the Nyquist criterion will be aliased to a lower spatial frequency, resulting in an error in the wave-front estimate. This term has a magnitude of about one third of the fitting error.[28]

The primary mirror segments are not phased before adaptive optics science nights; an estimate of the alignment of the segments is needed.

There are static calibration errors: The centroid offsets, system matrix and the DM-to-lenslet registration all have some error associated with them. In addition, there are dynamic calibration errors. As the spot size increases due to the seeing, the offset centroids no longer correspond to the same wave-front slope for which they were calibrated. This is accounted for to some degree by scaling the centroid offsets, but the scaling is not exact as each spot is of a different size at any given time.

### G. Summary of error terms

In calculating the error terms, the atmospheric turbulence is assumed to be Kolmogorov,[29] with a turbulence strength defined by $r_0$. Tests have shown that the Kolmogorov model of atmospheric turbulence describes the wave-front aberrations encountered at Keck Observatory well, with the exception of tip/tilt aberrations, which are augmented by telescope vibrations.[10] Hence, the measurements of $r_0$ are made from tip/tilt-removed images or centroid diagnostics.

It is important to emphasize that the individual wave-front errors are assumed to be statistically uncorrelated and hence their magnitudes are added in quadrature (*i.e.*, their variances are added). This means that small errors have a negligible effect on the total error budget in the presence of much larger terms.

Many images and diagnostics were taken on June 15, 2003. From the Strehl of the images, the RMS wave-front error was estimated to be 260 nm. It was estimated that $r_0$ at 500 nm was 18 cm.

To find all the total RMS wave-front error, the variances of all the individual terms are added

in quadrature:

$$\begin{aligned}\sigma_{\text{total}} &= \sqrt{\sigma^2_{\text{CAM}} + \sigma^2_{\text{FIT}} + \sigma^2_{\text{TEL}} + \sigma^2_{\text{TT-BW}} + \sigma^2_{\text{DM-BW}} + \sigma^2_{\text{TT-NOISE}} + \sigma^2_{\text{DM-NOISE}}} \\ &= \sqrt{113^2 + 139^2 + 60^2 + 75^2 + 103^2 + 9^2 + 17^2} \\ &= 229 \text{ nm.} \end{aligned} \tag{30}$$

It is reasonable to assume that the miscellaneous error terms presented in Sect. **3.F.** comprise the 125 nm needed to obtain the 260 nm of error estimated from the images.

## 4. Experimental results

Images of a number of stars under a variety of seeing conditions were captured between May 22 and June 16, 2003.

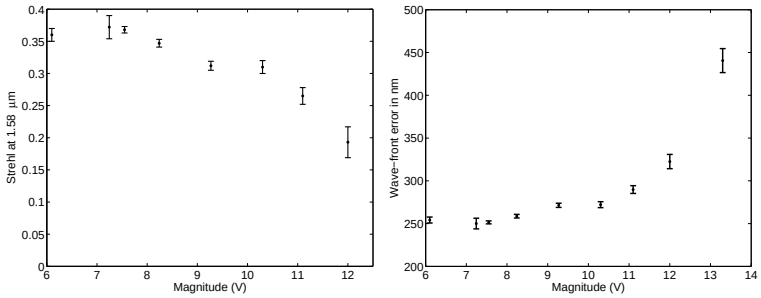


Fig. 5. Strehl ratio at 1.58 $\mu$m (left) and the RMS wave-front error obtained using the Maréchal approximation (right). The points represent the mean of about 10 images and the error bars represent the $1\sigma$ spread about the mean.

Figure 5 plots the Strehl using the H continuum (1.58 $\mu$m) filter as a function of guide star brightness and the corresponding RMS wave-front error from the Maréchal approximation. In each case, the optimum lenslet array plate scale, frame rate and loop gains were chosen. The FWHM of the best corrected images is 36.5 mas, while the best images on the magnitude 12 star had a FWHM of 40 mas. By comparison, the diffraction-limited FWHM is 33.6 mas. The magnitude 13.3 star in Fig. 5 was imaged at K' (2.12 $\mu$m) and hence is not included in the Strehl plot. The images had exposure times of between three and 20 seconds. The limiting magnitude of the AO system is about 14.

## 5. Conclusion

The AO system at Keck Observatory has been characterized. The AO system is shown to deliver images with an average Strehl ratio of up to 0.37 at 1.58 $\mu$m with a bright guide star. This corresponds to an wave-front error of 260 nm. A bright guide star error budget that is consistent with the observed image quality is presented. The major error terms on a bright guide star are the fitting error, the deformable mirror bandwidth errors and the internal calibration error, all of which are over 100 nm RMS. Of secondary importance are the tip/tilt bandwidth error and the telescope aberrations. The limiting magnitude of the AO system is 14, with rapid performance degradation for guide stars fainter than magnitude 12.

Fig. 6. Diffraction-limited image at 1.58 $\mu m$ (left), best bright star image (center) and best image of a magnitude 12 star (right).

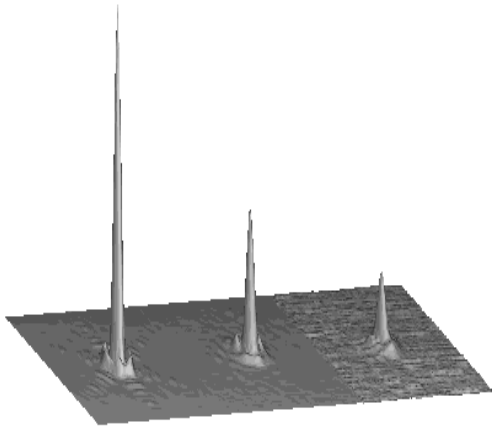


## Acknowledgements

This work was performed under the auspices of the US Department of Energy by the University of California, Lawrence Livermore National Laboratory, under contract W-7405-Eng-48. The work has been supported by the National Science Foundation Science and Technology Center for Adaptive Optics, managed by the University of California at Santa Cruz under cooperative agreement No. AST-9876783. The authors wish to thank the AO groups at both LLNL and Keck Observatory for their assistance.



M. A. van Dam may be reached at mvandam@igpp.ucllnl.org.


## References


1. F. Roddier, "Imaging through the atmosphere," in *Adaptive Optics in Astronomy*, ed. F. Roddier, Cambridge University Press, Cambridge (1999).
2. M. C. Roggemann and B. Welsh, *Imaging through turbulence*, CRC Press, Boca Raton, Fla. (1996).
3. J. W. Hardy, *Adaptive Optics for Astronomical Telescopes*, Oxford University Press, New York (1998).
4. P. L. Wizinowich, D. S. Acton, C. Shelton, P. Stomski, J. Gathright, K. Ho, W. Lupton, K. Tsubota, O. Lai, C. Max, J. Brase, J. An, K. Avicola, S. Olivier, D. Gavel, B. Macintosh, A. Ghez, J. Larkin, "First light adaptive optics images from the Keck II telescope: a new era of high angular resolution imagery," PASP **112**, 315-319 (2000).
5. M. Troy, R. G. Dekany, G. L. Brack, B. R. Oppenheimer, E. E. Bloemhof, T. Trinh, F. G. Dekens, F. Shi, T. L. Hayward, and B. R. Brandl, "Palomar adaptive optics project: status and performance," Proc. SPIE **4007**, 31-40 (2000).
6. F. Rigaut, D. Salmon, R. Arsenault, J. Thomas, O. Lai, D. Rouan, J. P. Véran, P. Gigan, D. Crampton, J. M. Fletcher, J. Stilburn, C. Boyer and P. Jagourel, "Performance of the Canada-France-Hawaii telescope adaptive optics Bonnette," PASP **110**, 152-164 (1998).
7. L. C. Roberts, Jr. and C. R. Neyman, "Characterization of the AEOS system," PASP **114**, 1260-1266 (2002).

8. D. Gavel, E. Gates, C. Max, S. Olivier, B. Bauman, D. Pennington, B. Macintosh, J. Patience, C. Brown, P. Danforth, R. Hurd, S. Severson, J. Lloyd, "Recent science and engineering results with the laser guidestar adaptive optics system at Lick Observatory," in *Adaptive Optical System Technologies II*, P. L. Wizinowich and D. Bonaccini, eds., Proc. SPIE **4839**, 354-359 (2003).
9. D. L. Fried, "Optical resolution through a randomly inhomogeneous medium for very long and very short exposures", J. Opt. Soc. Am. **56**, 1372-1379 (1966).
10. M. Schoeck, D. Le Mignant, G. Chanan, P. L. Wizinowich and M. A. van Dam, "Atmospheric characterization with the Keck adaptive optics system I: open-loop data," Applied Optics **42**, 3705-3720 (2003).
11. R. H. Hudgin, "Wave-front reconstruction for compensated imaging," J. Opt. Soc Am. **67**, 375-378 (1977).
12. B. L. Ellerbroek, personal communication (2002).
13. B. R. Oppenheimer, D. Palmer, R. G. Dekany, A. Sivaramakrishnan, M. A. Ealey, T. R. Price, "Investigating a Xinetics Inc. deformable mirror," in *Adaptive Optics and Applications*, R. K. Tyson and R. Q. Fugate, eds., Proc. SPIE **3126**, 569 (1997).
14. M. D. Oliker, "Alignment techniques for DM, lenslet, and WFS camera at the SOR," in *Adaptive Optics and Applications*, R. K. Tyson and R. Q. Fugate, eds., Proc. SPIE **3126**, 595-604 (1997).
15. D. S. Acton, P. L. Wizinowich, P. J. Stomski, J. C. Shelton, O. Lai, J. M. Brase, "Laboratory calibration of the W. M. Keck Observatory adaptive optics facility," in *Adaptive Optical System Technologies*, D. Bonaccini, R. K. Tyson, eds., Proc. SPIE **3353**, 125-131 (1998).
16. M. G. Loefdahl and G. B. Scharmer, "Wavefront sensing and image restoration from focused and defocused solar images," Astron. Astrophys. Suppl. Ser. **107**, 243-264 (1994).
17. R. J. Noll, "Zernike polynomials and atmospheric turbulence," J. Opt. Soc. Am. **66**, 207-211 (1976).
18. J-P. Véran and G. Herriot, "Centroiding gain compensation in Shack-Hartmann adaptive optics systems with natural or laser guide star," J. Opt. Soc. Am A **17**, 1430-39 (2000).
19. P. J. Stomski, Jr. and J. C. Shelton, "Compensating for pupil rotation in the W. M. Keck Observatory adaptive optics system," in *Adaptive Optical Systems Technology*, P. L. Wizinowich, ed., Proc. SPIE **4007**, 608-619 (2000).
20. N. F. Law and R. G. Lane, "Wavefront estimation at low light levels," Optics Comms **126**, 19-24 (1996).
21. P.-Y. Madec, "Control techniques," in *Adaptive Optics in Astronomy*, pp 131-54, ed. F. Roddier, Cambridge University Press, Cambridge (1999).
22. P. D. Stroud, "Diffraction and scintillation of laser beams by atmospheric turbulence," Los Alamos National Laboratory Note LAUR-93-1401 (1993).
23. R. Gerchberg and W. Saxton "A practical algorithm for the determination of phase from image and diffraction plane picture", Optik **35**, 237-246 (1972).
24. R. G. Lane, W. R. Fright and R. H. T. Bates, "Direct phase retrieval," IEEE Trans. Acoust., Speech, Signal Processing, **ASSP-35**, 520-526 (1987).
25. S. E. Winters, "Modeling and control of a deformable mirror," Journal of Dynamic Systems, Measurement, and Control **124**, 297-302 (2002).
26. G. Chanan, C. Ohara and M. Troy, "Phasing the mirror segments of the Keck telecopes II: the narrow band phasing algorithm," Applied Optics **39**, 4706-4714 (2000).
27. E. M. Johansson, D. S. Acton, J. R. An, K. Avicola, B. V. Beeman, J. M. Brase, C. J. Carrano, J. Gathright, D. T. Gavel, R. L. Hurd, O. Lai, W. Lupton, B. A. Macintosh, C. E. Max, S. S. Olivier, J. C. Shelton, P. J. Stomski, K. Tsubota, K. E. Waltjen, J. A. Watson and P. L. Wizinowich, "Initial performance of the Keck AO wavefront controller system," in *Adaptive Optical Systems Technology*, P. L. Wizinowich, ed., Proc. SPIE Vol. 4007, 600-607 (2000).
28. F. J. Rigaut, J.-P. Véran and O. Lai, " Analytical model for Shack-Hartmann-based adaptive optics systems", in *Adaptive Optical System Technologies*, D. Bonaccini and R. K. Tyson, eds., Proc. SPIE **3353**, 1038-1048 (1998).
29. F. Roddier, "The effect of atmospheric turbulence in optical astronomy", *Progress in Optics*, E. Wolf, ed. (North-Holland, Amsterdam, 1981), pp. 283-376.